communications physics

ARTICLE

https://doi.org/10.1038/s42005-023-01241-w OPEN

Insight on charge-transfer regimes in electron-phonon coupled molecular systems via numerically exact simulations

Michel Panhans[1,2], Sebastian Hutsch[1,2] & Frank Ortmann[1,2]✉

Various simulation approaches exist to describe charge transport in organic solids, offering significantly different descriptions of the physics of electron-phonon coupling. This variety introduces method-dependent biases, which inevitably result in difficulties to interpret charge transport processes in a unified picture. Here, we combine numerical and analytical quantum approaches to investigate the charge-transfer dynamics in an unbiased framework. We unveil the fading of transient localisation and the formation of polarons in a broad range of vibrational frequencies and temperatures. By studying the joint electron-phonon dynamics from femtoseconds to nanoseconds, we identify three distinct charge-transport regimes: transient localisation, Soft Gating, and polaron transport. The dynamic transitions between such regimes are ruled by a buildup of the correlations between electronic motion and nuclei, which lead to the crossover between transient localisation and polaron transport. This transition is seamless at all temperatures and adiabaticities, even in the limit of low-frequency vibrational modes.

[1] TUM School of Natural Sciences, Department of Chemistry, Technische Universität München, 85748 Garching b, München, Germany. [2] Center for Advancing Electronics Dresden, Technische Universität Dresden, 01062 Dresden, Germany. ✉email: frank.ortmann@tum.de

The thorough understanding of the interplay of electronic motion and nuclear vibrations with their characteristic time scales is a challenging fundamental task in many domains of condensed matter research[1–3] with great relevance for modern materials for energy conversion, comprising electronic materials such as oxides, halide perovskites, and organic semiconductors (OSCs)[4–6]. For these materials, vibrations play an important role because the electron–phonon coupling (EPC) impacts almost all electronic and optoelectronic features, relaxation processes and charge-carrier transport[5,7–12]. Despite considerable research efforts, a consistent non-perturbative transport theory covering the whole range of possible vibration modes does not exist, and for different OSC materials such as naphthalene[13], rubrene[14,15] and other OSC materials[16], different theoretical approaches are used. Various numerical schemes have been studied in recent years and improved upon different aspects of the problem[14,17–27]. Each of these approaches is associated with a specific regime of the so-called adiabaticity parameter α that relates electronic and vibrational energies (*vide infra*). For the adiabatic case (small α), one may treat the EPC effectively with a vibrational disorder potential as in the transient localisation (TL) scenario[10,14,28] or other adiabatic models[29,30]. The opposite so-called anti-adiabatic limit is the basis of (analytic) polaron and hopping theories[13,31–37]. Recent progress for a more consistent description of the vibrations includes the introduction of non-adiabatic effects by surface hopping schemes[24,38], a time-consistent hopping approach[39] or a mode-specific treatment of the vibrations[26,27,40]. Despite this progress, however, treatment of all modes on equal footing within a quantum framework remains a great challenge because of the large range of possible α values. This phase space between the two limiting cases of α is crowded by a large number of material systems, and most systems cannot be clearly assigned to one or the other limiting case—the main challenge for our understanding. Addressing these questions, one realises that the challenge even exists for a prototypical minimal model, the two-site Holstein model, which has a long history in theoretical research[41]. Maybe surprising at first glance, the reason is that the two-site Holstein model is the very basis for introducing the adiabaticity parameter $\alpha = \hbar\omega_{\mathrm{ph}}/\varepsilon_{12}$ with the transfer integral ε_{12} between the two sites and the frequency of vibrations ω_{ph} on each site. This model is, therefore, central to the understanding of the crossover regime with intermediate α values.

In this work, we analyse the vibration-coupled charge-carrier dynamics in the prototypical two-site Holstein model and find different charge-transport regimes that emerge from the interplay of electronic transfer integrals and the EPC energies. By simulating the electron's exact quantum dynamics (EQD) for different adiabaticities and temperatures, we provide insights into the seamless transition between theories for limiting cases. We relate the charge-carrier dynamics to the dynamics of the phonon modes and identify signatures of both types of particles in both the electronic and the phononic spectra. We identify three different regimes in the charge-transfer dynamics, which are the regime of TL, Soft Gating (SG), and polaron transport. For all regimes, we extract their corresponding time scales and discuss their impact on carrier transport. These detailed insights into the dynamical evolution of electron-phonon coupled systems provide a better general understanding of carrier-transport mechanisms in OSCs and related systems beyond limiting cases of the adiabaticity parameter.

Results and discussion

Modelling and numerically exact simulations. In the two-site Holstein Hamiltonian, which serves as a model for the charge transfer between two molecules or two electronic states in general, the electronic states are locally coupled to molecular vibrations as described by

$$\begin{aligned}\hat{H}_{\mathrm{Hol}} =& \hat{H}_{\mathrm{el}} + \hat{H}_{\mathrm{el-ph}} + \hat{H}_{\mathrm{ph}} = \varepsilon_{12}\left(\hat{c}_1^{\dagger}\hat{c}_2 + \hat{c}_2^{\dagger}\hat{c}_1\right) \\ &+ \sum_{i=1}^{2}\hbar\omega_{\mathrm{ph}}g\left(\hat{b}_i^{\dagger} + \hat{b}_i\right)\hat{c}_i^{\dagger}\hat{c}_i + \sum_{i=1}^{2}\hbar\omega_{\mathrm{ph}}\left(\hat{b}_i^{\dagger}\hat{b}_i + \frac{1}{2}\right).\end{aligned} \tag{1}$$

Here, ε_{12} is the electronic transfer integral between the sites and $\hbar\omega_{\mathrm{ph}}$ is the energy of the vibration mode (taken equal for the same type of molecules). The EPC is given by a dimensionless coupling constant g, and we set $\varepsilon_{11} = \varepsilon_{22} = 0$ to focus on the interplay between the electronic coupling and the EPC. To describe charge transfer, we simulate the optical conductivity $\sigma(\omega)$ of the system and the mean square displacement (MSD) $\Delta x^2(t)$ of the electron, which is a central quantity in the theoretical description of charge- and energy transfer[14,42–44]. The connection between both is given by the Kubo formula for longitudinal charge transport[45,46] by means of an Einstein relation,

$$\Re\left(\sigma_{xx}(\omega)\right) = \frac{e^2\beta}{4V}\frac{\tanh\left(\frac{\beta\hbar\omega}{2}\right)}{\frac{\beta\hbar\omega}{2}}\int_{-\infty}^{\infty}dt e^{-i\omega t}\frac{d^2}{dt^2}\Delta x^2(t). \tag{2}$$

To include variable temperatures, we study the EQD of this system by evaluating the thermally averaged electronic MSD for a single electron,

$$\Delta x^2(t) = \mathrm{Tr}_{\mathrm{1el}}\left(\hat{\rho}_0\Delta\hat{x}^2(t)\right), \tag{3}$$

with spatial displacement $\Delta\hat{x}(t) = e^{it\hat{H}_{\mathrm{Hol}}/\hbar}\hat{x}(0)e^{-it\hat{H}_{\mathrm{Hol}}/\hbar} - \hat{x}(0)$ and the (canonical) density operator $\hat{\rho}_0 = e^{-\beta\hat{H}_{\mathrm{Hol}}}/\mathrm{Tr}_{\mathrm{1el}}(e^{-\beta\hat{H}_{\mathrm{Hol}}})$. The trace runs over the phononic degrees of freedom and over all one-electron states. The numerical evaluation of the MSD is performed by a linear-scaling quantum-transport method[44,47]. The implementation of the Holstein Hamiltonian is realised in electron-phonon product spaces using a phonon-space truncation method[48–50]. (see "Methods" section for technical details)

In the simulations for varying adiabaticity α, we fix the electronic coupling at $\varepsilon_{12} = 40$ meV. This energy serves as a reference energy scale here and is a typical value found in OSCs[10,19,24,39,51]. We then vary $\hbar\omega_{\mathrm{ph}}$ and g such that the molecular relaxation energy $\Lambda = \hbar\omega_{\mathrm{ph}}g^2 = 80$ meV is kept constant. This has the advantage that the interaction energy is always the same, while α varies in the range $0.125 \le \alpha \le 5.0$ (see Supplementary Table 1), which covers the known limits, i.e. TL (smallest α) and small polarons (large α). At this point, we note that in particular for small mode energies and large EPC constants, the present model might be extended in the future by anharmonic effects in the vibration dynamics and non-linear EPC terms, which may become relevant for organic molecular crystals[52,53] and lead-halide perovskites[54,55]. We also note that all results are qualitatively unaffected by rescaling all energies as only their relative values are relevant for the qualitative behaviour. We start discussing our results for short evolution times up to several tens of fs, where the features support the previously described TL scenario[10,14].

Exact dynamics at transient-localisation time scales. We first simulate the MSD with EQD for short times and compare different vibration energies $\hbar\omega_{\mathrm{ph}}$ in Fig. 1a (with a_0 the distance between the sites). We observe qualitatively different electron-transfer dynamics in dependence on the mode energy between 5 meV and 200 meV, which are chosen to be well below and well above the reference transfer integral of 40 meV, respectively. After an initial behaviour (up to ~20 fs), the curves diversify greatly at later times. For clarity in the figure, not all curves are shown for all times. We find that in the case of the slowest mode (5 meV, black

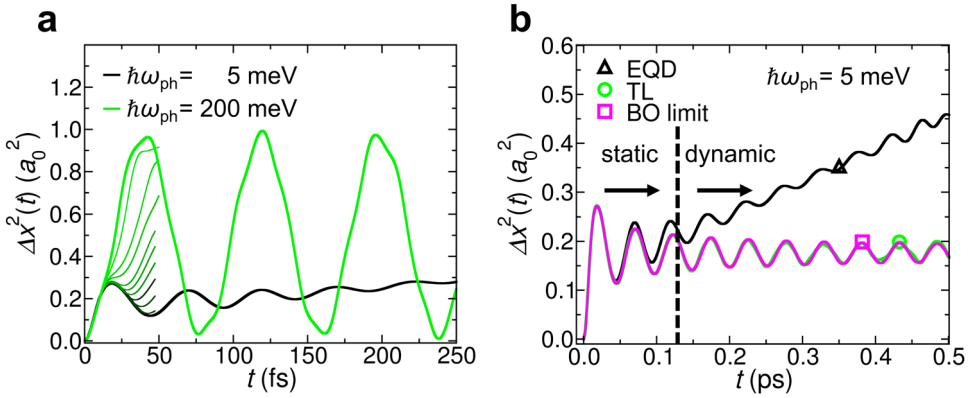

Fig. 1 Short-time exact-quantum-dynamics–mean-square-displacement (EQD–MSD) simulations. a Short-time behaviour for the considered range of vibration mode energies $\hbar\omega_{ph}$ (MSD data for intermediate values of mode energies are only indicated up to 50 fs for clarity). **b** Identification of transient localisation (TL) within the static limit of the electron–phonon coupling (green curve, open circle) as discussed in the main text and evaluated in the "Methods" section. The MSD based on the adiabatic Born-Oppenheimer (BO) limit (magenta curve, open square) is shown for comparison (see Eq. (S27) in Supplementary Note 2).

curve in Fig. 1a), the MSD increases slowly with time after ~130 fs. This gradual increase is accompanied by a reduced oscillatory modulation. For the fastest mode (200 meV), in contrast, the MSD shows strong periodic oscillations. This case is qualitatively similar to the completely uncoupled case, for which the analytical result $\Delta x^2(t) = \frac{a_0^2}{2}\left(1-\cos\left(\frac{2\varepsilon_{12}t}{\hbar}\right)\right)$ has a periodicity of $\pi\hbar/\varepsilon_{12} = 52$fs. Quantitatively, however, this period differs from the numerically observed period in Fig. 1a, which will be discussed further below.

We first focus on the low-frequency case ($\alpha < 1$). To understand the charge-transfer dynamics for $\hbar\omega_{\rm ph} = 5$ meV in more detail, we relate it to the charge-transfer dynamics obtained from the static limit of EPC (see "Methods" section for details). In this limit, the EPC manifests in a vibration-induced electronic disorder potential $\hat{V}(T) = \sum_i \hbar\omega_{\rm ph} g(1+2n_{\rm ph})^{1/2}\phi_i \hat{c}_i^\dagger \hat{c}_i$, where i runs over all electronic sites, and ϕ_i is a normalised Gaussian random variable. This purely electronic disorder model corresponds to the TL scenario for low-energy modes and is compared to the approximation-free EQD in Fig. 1b. The MSD in the TL simulation is similar to the one obtained with EQD up to an evolution time of around ~130 fs, which corresponds to $1/\omega_{\rm ph}$. At longer times in Fig. 1b, the transiently frozen modes cause the electron to localise, and the MSD saturates. For the exact dynamics, in contrast, we observe an increasing MSD. In TL approaches, this quantum localisation is usually actively suppressed via the relaxation-time approximation[10,14,28,40] with an effective relaxation time of $1/\omega_{\rm ph}$, leading to non-zero mobilities. In Fig. 1b, we have additionally plotted the analytic result for the MSD derived from the adiabatic Born-Oppenheimer approximation[29,30] (see Supplementary Note 2 for details) in magenta. The hardly distinguishable curves demonstrate its equivalence to the MSD from the static-disorder model for the chosen parameters.

Evidently, for modes with a small frequency, the range of validity of the static-disorder model is larger because the adiabaticity is small enough to justify this assumption for somewhat larger times. However, as the mode energy increases, this static description is unable to describe the EQD properly, as shown in Fig. 1b by the deviation of the MSD for longer times ($t > 130$ fs). While this interesting behaviour for longer times is discussed further below, we first keep our focus on early times and discuss the case of high-frequency modes ($\alpha > 1$).

Polaronic transport features. For high-frequency modes, the electron-transfer from EQD is analysed in Fig. 2a. We observe forth-and-back oscillations in the MSD (green curve in Fig. 2a) with a periodicity of 81.1 fs in the case of $\hbar\omega_{\rm ph} = 200$ meV, which would correspond to the MSD dynamics of an *effective electronic* two-site model described by $\left(1-\cos\left(2\gamma_{12}t/\hbar\right)\right)$. The extracted effective transfer integral is $\gamma_{12} = \pi\hbar/t_\gamma = 25.8$ meV. This value is very close to the renormalised (narrowed) transfer integral of $\tilde{\varepsilon}_{12} = e^{-g^2(1+2n_{\rm ph})}\varepsilon_{12} = 26.8$ meV calculated from analytical polaron theories[13,31,36]. The EQD-MSD (green curve in Fig. 2a) is compared to the analytical result (magenta curve in Fig. 2a) obtained from polaron theory (see Eq. (M8) in the Methods section). Both the EQD and the analytical result match well due to the similar effective transfer integrals. On the other hand, the dashed grey curve in Fig. 2a corresponds to the case of vanishing EPC (with the bare ε_{12}) and shows more rapid oscillations. From the comparison of these results for the bare and analytically narrowed transfer integrals, we conclude that the charge-transfer dynamics is polaronic in nature, and the period (and renormalisation), as predicted by polaron theory, is closely matched.

Starting from this clear-cut polaronic case, we next study how the polaronic renormalisation effect develops when the mode energy is smaller, and we extend the numerical calculations to much larger times and lower temperatures. Figure 2b, c shows exemplary results when $\hbar\omega_{\rm ph}$ has dropped below the transfer integral (i.e. $\hbar\omega_{\rm ph} = 20$ meV and 10 meV). For such low-frequency modes, polaronic effects are usually assumed to be absent because the adiabaticity parameter is below 0.5. Unexpectedly, even for these modes, we do observe strong oscillations with polaronic character in the EQD–MSDs. For a temperature of 10 K, for example, the oscillations exhibit large amplitudes that are dominated by periods of $t_\gamma = 1.4$ ps in Fig. 2b and 12.9 ps in Fig. 2c. These periods correspond to effective transfer integrals of $\gamma_{12} = 1.47$ meV and 0.16 meV, respectively, and are more than one order of magnitude smaller than the bare electronic values and thus polaronic in nature. The EQD–MSD at 300 K (Fig. 2b, c) reveals that these reduced effective transfer integrals are quite independent of temperature.

We further emphasise that this behaviour is not described by the renormalisation factors of analytic or variational polaron theories[13,31,36,56,57], that predict an exponential decrease with phonon occupation $n_{\rm ph}$ according to the analytical values $e^{-g^2(1+2n_{\rm ph})}$ or the variational values $e^{-\phi_{sc}^2(1+2n_{\rm ph})}$ (variational coupling constant ϕ_{sc}, see Supplementary Note 3 for details on variational approaches to the two-site Holstein model) and are strongly temperature dependent for the values considered here.

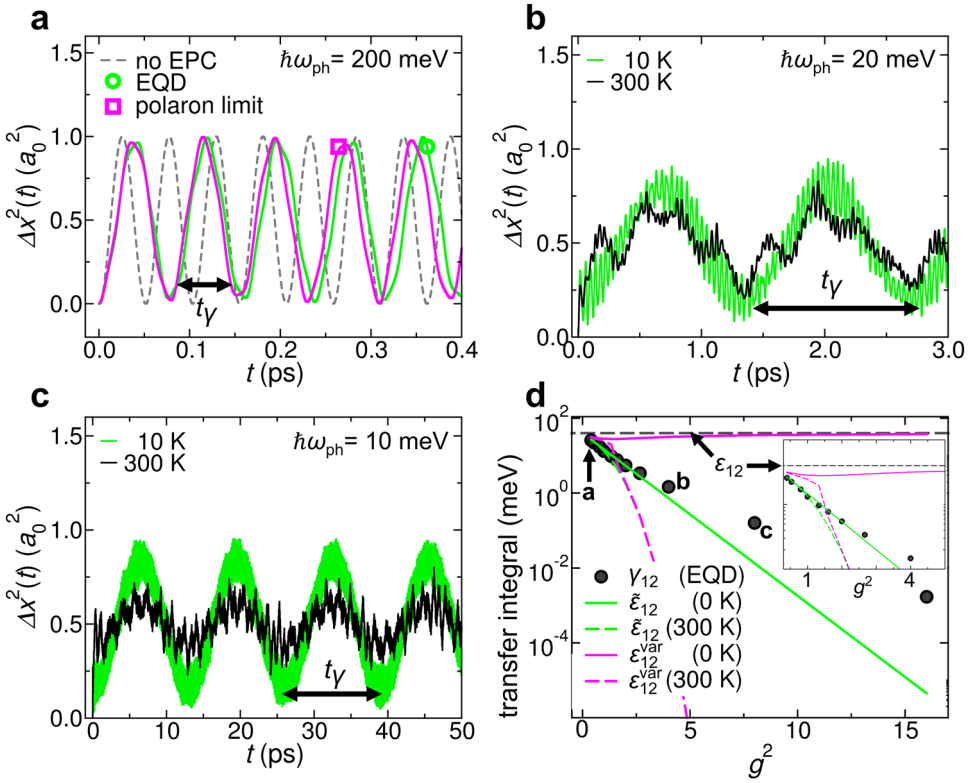

Fig. 2 Polaronic transport features at different temperatures. a Comparison of the MSD based on polaron theory (magenta, open square) and formation of polaronic oscillations in the EQD-MSD (green, open circle). The dashed grey curve is the zero-EPC result (see main text). **b** MSD for a mode energy of 20 meV and $g = 2.0$ at two different temperatures. **c** Same as in **b** but with $\hbar\omega_{ph} = 10$ meV and $g = 2.83$. **d** Extracted polaronic transfer integrals γ_{12} at 300 K as a function of the EPC coupling strength g^2 (full circles) in comparison to analytical values of the renormalised, variational, and bare transfer integrals $\widetilde{\varepsilon}_{12}$ (green), $\varepsilon_{12}^{\mathrm{var}}$ (magenta, see Eq. (S46) in Supplementary Note 3), and ε_{12} (dashed grey line). The labels **a**–**c** inside the plot correspond to the values of γ_{12} extracted from the MSD shown in Fig. 2a–c. The inset in **d** zooms into the range of $0.6 \leq g^2 \leq 4$ for better comparison.

In contrast, this reduction is not observed in the MSD for none of the shown mode energies.

In order to investigate the generality of these results, we further extend our scope in Fig. 2d to many more frequencies, where we plot the extracted effective transfer integrals γ_{12} (obtained at 300 K) as black dots versus the EPC coupling strength g^2 and compare them to the renormalised transfer integrals $\widetilde{\varepsilon}_{12}$ at 0 and at 300 K (solid and dashed green lines). We find that for mode energies above 10 meV, the effective polaronic oscillations of the exact MSDs are nicely described with the renormalised transfer integrals at zero temperature given by $\varepsilon_{12}e^{-g^2}$ (solid green line, see also inset of Fig. 2d). In contrast, for 5 meV and 10 meV the numerical values are much larger than the analytical reference value by factors of 400 and 10, respectively. Furthermore, we also include results for the effective transfer integrals obtained from variational polaron theories[56,57] (solid and dashed magenta lines), which we have applied to the two-site Holstein model. From the comparison with the effective variationally obtained transfer integrals $\varepsilon_{12}^{\mathrm{var}} = \varepsilon_{12}e^{-\phi_{\mathrm{sc}}^2}$ (solid magenta line in Fig. 2d) at zero temperature, we do not find any relation to γ_{12} obtained from the EQD. The discrepancy between the analytic (variational) effective transfer integrals and the effective transfer integral γ_{12} illustrates that transport properties (such as the MSD) are not directly accessible from simple polaronic energy parameters. Thus, charge-transport needs to be evaluated independently, as also found in variational polaron theories[57].

In any event, the strong difference to the bare transfer integral (dashed grey line in Fig. 2d) proves the existence of polaron transport on picosecond time scales, and we observe its independency of the adiabaticity parameter $\hbar\omega_{\mathrm{ph}}/\varepsilon_{12}$. This is a central finding of the present work. We conclude that the main oscillation periods in the MSD are of polaronic nature for all studied vibrational mode energies and all studied temperatures. This insight may be used in future theories for the long-time charge dynamics in the presence of EPC independently of the adiabaticity. This is particularly important for the possible improvement of TL theory, which currently does not take into account dynamical effects after the TL time.

Our simulations further show that after the emergence of polaronic transport features discussed above, the system does not show additional dynamical regimes at even later times (see Supplementary Fig. 3 for a dynamical evolution at the nanosecond scale). This observation can be identified with an already *completely formed polaron* (at low and at high temperatures). Turning back to the ultrafast timescales, the central questions are how the formation process of the polaron proceeds and how the TL fades away? Therefore, the time evolution of the correlated electron-phonon dynamics between TL and polaron transport is of particular interest.

Intermediate transport regime and SG. The quantum dynamics after the static regime and before the long-time regime (polaron limit) are notoriously difficult to access and evades a precise analytical description. We investigate the MSD for these intermediate times at exemplary temperatures of 10 and 300 K. This intermediate charge-transport regime is best visible if the time difference between the initial phase and the long-time regime is large enough, i.e., the polaronic oscillations have a large oscillation period due to strong renormalisation of the transfer integrals.

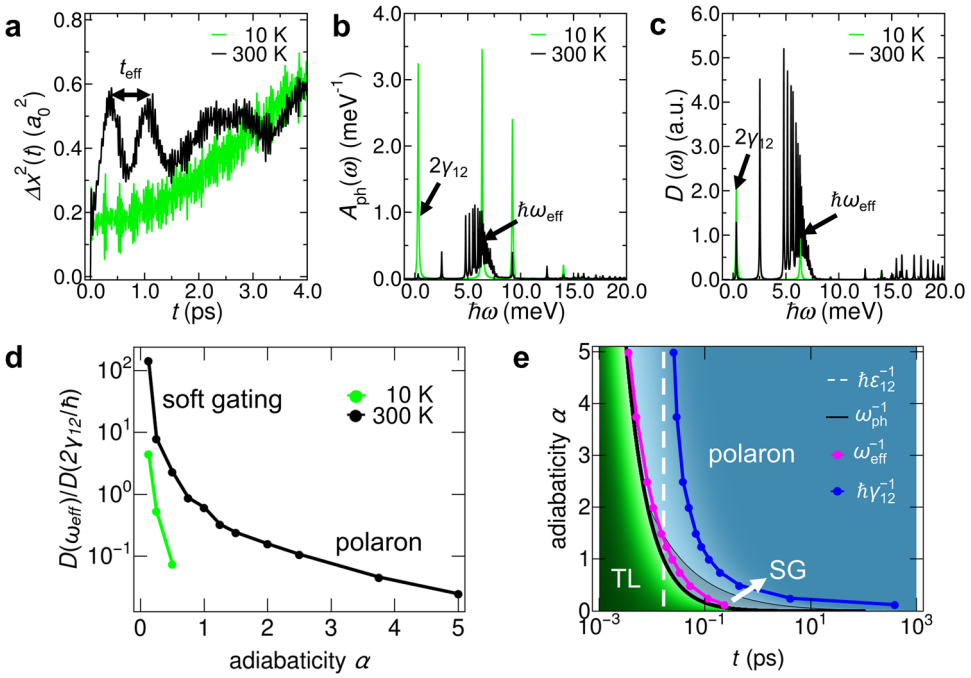

Fig. 3 Time- and energy-resolved charge-transfer dynamics of three different charge-transport regimes at low and elevated temperatures. a Mean square displacement (MSD) for intermediate times up to 4 ps for $\hbar\omega_{ph} = 10$ meV and $g = 2.83$. **b** Phonon spectral function $A_{ph}(\omega)$ obtained from Eq. (4) for $\hbar\omega_{ph} = 10$ meV and $g = 2.83$. **c** Low-frequency spectrum of the diffusion coefficient $D(\omega)$, which is obtained from the time-dependent diffusion coefficient $D(t) = \frac{d}{dt}\Delta x^2(t)$ as the time derivative of the MSD displayed in panel (**a**). **d** Relative peak height $D(\omega_{eff})/D(2\gamma_{12})$ as a function of the adiabaticity and for different temperatures. The relative peak heights for 10 K are only plotted for the lowest vibrational frequencies due to the absence of a peak at ω_{eff} for frequencies larger than 20 meV. **e** Comparison of effective time scales for transient localisation (TL), Soft Gating (SG), and polaron transport given by ω_{ph}^{-1} (black), ω_{eff}^{-1} (magenta), and γ_{12}^{-1} (blue) for all adiabaticities. The temperature in **e** is fixed at 300 K. The dashed vertical line indicates the time scale of charge transport without electron–phonon coupling. The colour gradients indicate the regions where TL (green colour gradient) and polaron transport (white-blue colour gradient) take place in the charge-transfer dynamics. The semi-transparent grey area indicates the SG regime.

This is best seen in the case of $\hbar\omega_{ph} = 10$ meV, which we select for the following discussion.

Figure 3 summarises the results obtained for the EQD–MSD. At small times, Fig. 3a shows the increase of the MSD, which indicates the lifting of TL that was observed in Fig. 1 below 100 fs. While this occurs for both temperatures, the concrete dynamics is qualitatively different for both cases. At low temperature and after the TL time of $\omega_{ph}^{-1} = 65.8$ fs, the MSD does not exhibit the oscillations that appear at higher temperatures in the time window $\omega_{ph}^{-1} < t < 1.5$ ps (black). Therefore, the difference in the dynamical behaviours must be caused by the finite temperature and can be explained as follows.

From the dynamical evolution of the system at 300 K in Fig. 3a, we find that the dominant oscillations in the MSD are related to the vibration period of the modes. We extract a period of $t_{eff} = 0.73$ ps, which corresponds to an energy of $\hbar\omega_{eff} = 5.8$ meV. The relation to the vibration, however, is not immediately obvious because this is only 58% of the nominal mode energy ($\hbar\omega_{ph} = 10$ meV) and, at first glance, it is not evident if both energies are related at all. To understand this connection, we study the phonon spectral function and compare it to the optical-electronic conductivity. In general, the phonon spectral function is defined as the imaginary part of the retarded Green's function (mode index λ)[58],

$$A_{ph}(\omega,\lambda) = -\frac{1}{\pi}\Im\left(G_{ph}^{ret}(\omega,\lambda)\right), \tag{4}$$

with the conventional time-domain bosonic Green's function $G_{ph}^{ret}(t,\lambda) = -\frac{i}{\hbar}\Theta(t)\mathrm{Tr}_{el}(\hat{\rho}_0[\hat{b}_\lambda(t), \hat{b}_\lambda^\dagger(0)])$. The latter is evaluated numerically analogously to the electronic MSD in Eq. (3). Technically, one can calculate $A_{ph}(\omega)$ after a simple transformation in phonon space by introducing the phonon−relative coordinates (defined by $\hat{b}_\lambda = (\hat{b}_1 - \hat{b}_2)/\sqrt{2}$). Only this coordinate is coupled to the electron dynamics, while the centre-of-mass coordinate is effectively decoupled from the electrons (see Supplementary Note 1 for details).

The phonon spectral function is shown in Fig. 3b. At 300 K, we find that the main weight in $A_{ph}(\omega)$ is contained in the broad spectral feature directly above 5 meV, which sharpens at lower T to a phonon peak at $\hbar\omega_{eff} = 5.8$ meV in accordance with the electron MSD. Furthermore, $A_{ph}(\omega)$ has almost completely lost its weight at the original mode energy of $\hbar\omega_{ph} = 10$ meV. We therefore identify this lowering in energy as EPC-induced renormalisation of the phonon-mode energy. A similar effect has been described as phonon softening[59–62]. Already this occurrence of a principal phonon peak that agrees exactly with the MSD oscillations in Fig. 3a strongly suggests that the vibration controls the MSD dynamics.

To relate the phonon spectrum more closely to the dynamical electron-transfer behaviour in the intermediate regime, the Fourier transform of the electron's diffusion coefficient $D(\omega)$, which is directly proportional to the conductivity $\Re(\sigma_{xx}(\omega))$ given in Eq. (2), is analysed in the low-frequency region in Fig. 3c. There, we see that $D(\omega)$ exhibits the same spectral components as $A_{ph}(\omega)$. We note that the largest features in $D(\omega)$ appear at and around the renormalised mode energy of 5.8 meV. This very similar behaviour of the diffusion coefficient and the phonon spectral function in Fig. 3b leads us to the conclusion that the

renormalised mode drives the transfer of the electron at ambient temperatures, which can be interpreted as an SG process appearing on transient time scales up to 1–2 ps. SG in this sense means that the transfer of the electron is facilitated (gated) by the phonon mode and appears synchronised in time to the motion of the renormalised (softened) phonon frequency.

In contrast, at lower temperatures a different behaviour is observed (cf. Fig. 3a), which can be understood with the freeze out of the renormalised phonon mode. Indeed, Fig. 3c shows that the spectral weight of the diffusion coefficient around the effective mode energy $\hbar\omega_{\mathrm{eff}}$ is strongly decreased at 10 K. But the mode is not inactive at low T. TL is still rapidly lifted, leading to a gradual increase of the MSD with values that are almost independent of temperature at 3 – 4 ps. The dominating $D(\omega)$ peak at $2\gamma_{12}$ for 10 K reveals that this MSD increase is not a SG mechanism but is already of polaronic nature, i.e. the SG regime is suppressed at low T. Taking the relative peak heights $D(\omega_{\mathrm{eff}})/D\left(2\gamma_{12}/\hbar\right)$ at the renormalised phonon ($\hbar\omega_{\mathrm{eff}}$) and polaron ($2\gamma_{12}$) energies as a characteristic measure for their relevance, we observe in Fig. 3d the dominance of SG for adiabaticities around and below 0.5 (at 300 K). In all other cases polaron transport dominates over SG, in particular, for high-frequency modes and at low temperatures. Thus, the SG mechanism is a thermally activated effect that leads to an additional transport channel on the picosecond time scale.

Note that the emergence of gating modes induced by the EPC has been postulated in semiclassical approaches, where these modes have either been found as a result[39] or have been introduced as an assumption[63–65]. However, these gating processes are due to rigid phonons, i.e. there is no coherent back-action to the vibrations, which is an important qualitative difference from the SG mechanism described in this work.

We present a final comprehensive picture by plotting the relevant time scales for TL, SG, and polaron transport in Fig. 3e for all considered adiabaticities α. We emphasise that independently of α, all three regimes appear during the charge-carrier dynamics at ambient temperatures, but they occur at different absolute times relative to our reference time scale ε_{12}^{-1} of the bare transfer integral (vertical dashed line). While TL is characterised by the sole electron dynamics at the smallest time (green colour gradient), it is replaced by correlated electron-phonon dynamics at intermediate times. Correlated motion continues in this intermediate regime in which SG (semi-transparent grey area) and the polaron formation (white-blue colour gradient) take place. This formation is eventually completed at γ_{12}^{-1} (blue points). All three regimes can be relevant for the charge-carrier dynamics in materials because they occur around the typical reference time scale ε_{12}^{-1}. This is eventually controlled by the adiabaticities. For low α, polaron transport, with its strong renormalisation effects, plays a minor role, and TL determines the carrier dynamics on the sub-hundred-femtosecond time scale. At intermediate values of α one observes mainly correlated electron-phonon dynamics and polaron formation. This dependence on α points out the importance of separating the vibrational spectrum into different parts to accurately include the impact of EPC on the carrier dynamics.

Conclusions

In summary, we have investigated the rich charge-carrier dynamics resulting from different time scales and varying material parameters in the prototypical two-site Holstein Hamiltonian and found three regimes of charge transport, namely the TL regime, the SG-transport regime, and polaronic transport. Furthermore, we obtained effective polaronic transfer integrals from the long-time carrier dynamics that are different to the ones established in the literature. We also extracted effective and renormalised phonon-mode energies, which determine the dynamics of the highly non-classical SG regime, which is observed at ambient temperatures but suppressed at low T. These fundamental insights help unify the understanding of electron-phonon coupled systems, which is currently relying on limiting cases of the adiabaticity parameter and should be a reference for better analytical models. This offers an intriguing perspective to study more complex systems such as organic crystals and other electron-phonon coupled systems in the future.

Methods

Electron–phonon product spaces. The numerical evaluation of the MSD is performed in electron-phonon product spaces, which includes the dynamical evolution of both electronic and phononic degrees of freedom. In the present case, we have implemented the one-electron–multiple-phonon Hilbert space for the two-site Holstein model of Eq. (1). The practical realisation of a sufficiently large electron–phonon product spaces requires a closer look on the parameters of the considered model. When considering large coupling strengths (up to $g = 4.0$) and low mode energies, which lead to large occupation numbers at 300 K, we must consider a large phonon space for the numerical calculations. To get reliable numerical results, we consider a truncated phonon space with a total maximum occupation of 100 vibrational levels, i.e., in minimum, there are 50 oscillator energy levels available for each site. The Hilbert-space dimension of this phonon subspace is 5151. This choice guarantees that there are enough oscillator levels available even for the highest possible thermal and EPC-induced occupation numbers. For the lowest mode energy of 5 meV, the thermal occupation at 300 K is 4.7. Additionally, the EPC-induced average occupation of the free oscillator energy levels is 16 due to the large value of g^2. A minimum oscillator-level number of 50 per site is thus sufficient to converge the numerical results. Since the applied algorithm uses a stochastic approach to calculate the trace (random-phase state) and to model thermal averages in the one-electron multiple-phonon subspace, we average over 768 statistically independent two-site models to converge this thermal average. Thus, the total system size corresponds to $768 \times 2 \times 5151 = 7.9 \times 10^6$.

For the dynamical evolution of the MSD in the electron-phonon product space (see Eq. (3) of the main text), we apply a time step of 0.1 fs, which is sufficiently small to resolve all relevant (high-energy) modulations in the quantum dynamics. Furthermore, the largest evolution times reaches up to 2.15 ns covering the slowest charge-transfer dynamics of the model.

The static limit of EPC. The static limit of the EPC is based on a separation of the vibrational modes in the Hamiltonian yielding

$$\Delta x^2_{\mathrm{stat}}(t) = \frac{\mathrm{Tr}_{\mathrm{el}}(e^{-\beta\hat{H}_{\mathrm{ph}}} e^{-\beta\left(\hat{H}_{\mathrm{el}}+\hat{H}_{\mathrm{el-ph}}\right)}\Delta\hat{x}^2_{\mathrm{stat}}(t))}{\mathrm{Tr}_{\mathrm{el}}(e^{-\beta\hat{H}_{\mathrm{ph}}} e^{-\beta\left(\hat{H}_{\mathrm{el}}+\hat{H}_{\mathrm{el-ph}}\right)})}, \tag{M1}$$

with

$$\Delta\hat{x}_{\mathrm{stat}}(t) = e^{\frac{it\left(\hat{H}_{\mathrm{el}}+\hat{H}_{\mathrm{el-ph}}\right)}{\hbar}}\hat{x}(0)e^{-\frac{it\left(\hat{H}_{\mathrm{el}}+\hat{H}_{\mathrm{el-ph}}\right)}{\hbar}} - \hat{x}(0), \tag{M2}$$

where we see that the phonons do not enter the time evolution any further.

One can analytically show that if we consider an ensemble of multiple but independent two-site Holstein models (e.g., uncoupled pairs of molecules), the EPC can be substituted with a vibrational disorder potential $\hat{V}(T)$, which does not contain any phononic degrees of freedom. This potential reads,

$$\hat{V}(T) = \sum_i \hbar\omega_{\mathrm{ph}} g\sqrt{1+2n_{\mathrm{ph}}}\,\phi_i\hat{c}_i^\dagger\hat{c}_i, \tag{M3}$$

where n_{ph} is the Bose occupation of the vibrational mode and ϕ_i is a normalised Gaussian random variable with standard deviation one. For this case, the MSD reads

$$\Delta x^2_{\mathrm{dis}}(t) = \frac{\mathrm{Tr}_{\mathrm{el}}(e^{-\beta\left(\hat{H}_{\mathrm{el}}+\hat{V}(T)\right)}\Delta\hat{x}^2_{\mathrm{dis}}(t))}{\mathrm{Tr}_{\mathrm{el}}(e^{-\beta\left(\hat{H}_{\mathrm{el}}+\hat{V}(T)\right)})}, \tag{M4}$$

with

$$\Delta\hat{x}_{\mathrm{dis}}(t) = e^{\frac{it\left(\hat{H}_{\mathrm{el}}+\hat{V}(T)\right)}{\hbar}}\hat{x}(0)e^{-\frac{it\left(\hat{H}_{\mathrm{el}}+\hat{V}(T)\right)}{\hbar}} - \hat{x}(0). \tag{M5}$$

The approximation in Eq. (M4) is compared to the full MSD given in Eq. (3) of the main text.

Velocity auto-correlation function and MSD in the polaron limit. In general, the MSD and the velocity auto-correlation function (VACF) are related by

$$\frac{d^2}{dt^2}\Delta x^2(t) = 2\Re\left(\mathrm{Tr}_{\mathrm{el}}\left(\hat{\rho}_0\hat{v}_x(0)\hat{v}_x(t)\right)\right), \tag{M6}$$

which is obtained by differentiation and cyclic permutation under the trace of $\Delta x^2(t)$.

The VACF in the polaron limit is derived as,

$$\Re\left(\mathrm{Tr}_{\mathrm{el}}\left(\hat{\rho}_0\hat{v}_x(0)\hat{v}_x(t)\right)\right)=\frac{1}{2}\left(\frac{\widetilde{\varepsilon}_{12}a_0}{\hbar}\right)^2\sum_{n=-\infty}^{\infty}I_n(x)e^{\frac{\beta\hbar\omega_{\mathrm{ph}}n}{2}}\Big((1-(-1)^n)\cos\left(n\omega_{\mathrm{ph}}t\right)+\frac{(1+(-1)^n)}{2}\left(\cos\left(\left(n\omega_{\mathrm{ph}}+\frac{2\widetilde{\varepsilon}_{12}}{\hbar}\right)t\right)+\cos\left(\left(n\omega_{\mathrm{ph}}-\frac{2\widetilde{\varepsilon}_{12}}{\hbar}\right)t\right)\right)\Big),\tag{M7}$$

where $\widetilde{\varepsilon}_{12}=\varepsilon_{12}e^{-g^2\left(1+2n_{\mathrm{ph}}\right)}$ is the so-called renormalised transfer integral[13,31,36], n_{ph} is the Bose occupation of the mode, and $I_n(x)$ are the modified Bessel functions of the first kind with the argument $x=4g^2\sqrt{n_{\mathrm{ph}}\left(1+n_{\mathrm{ph}}\right)}$. With the identity in Eq. (M6), we can easily determine the MSD based on the analytical result in Eq. (M7) as

$$\Delta x^2(t)=\left(\frac{\widetilde{\varepsilon}_{12}a_0}{\hbar}\right)^2\sum_{n=-\infty}^{\infty}I_n(x)e^{\beta\hbar\omega_{\mathrm{ph}}n/2}\left[(1-(-1)^n)\frac{(1-\cos(n\omega_{\mathrm{ph}}t))}{n^2\omega_{\mathrm{ph}}^2}+\frac{(1+(-1)^n)}{2}\left(\frac{\left(1-\cos\left(\left(n\omega_{\mathrm{ph}}+\frac{2\widetilde{\varepsilon}_{12}}{\hbar}\right)t\right)\right)}{\left(n\omega_{\mathrm{ph}}+\frac{2\widetilde{\varepsilon}_{12}}{\hbar}\right)^2}+\frac{\left(1-\cos\left(\left(n\omega_{\mathrm{ph}}-\frac{2\widetilde{\varepsilon}_{12}}{\hbar}\right)t\right)\right)}{\left(n\omega_{\mathrm{ph}}-\frac{2\widetilde{\varepsilon}_{12}}{\hbar}\right)^2}\right)\right],\tag{M8}$$

which is used to plot the MSD (normalised to a_0^2) in Fig. 2a (magenta curve, open square) of the main text. This relation represents one reference model to be compared to the numerical results of the MSD for the two-site Holstein model in Eq. (1) of the main text.

Data availability

The data that support the findings of this study are available from the corresponding author on reasonable request. Digital access to the data of the figures is possible via: https://doi.org/10.5281/zenodo.7752215.

Code availability

The custom codes used for the simulations are available from the corresponding author upon reasonable request.

Received: 13 January 2023; Accepted: 18 May 2023;
Published online: 31 May 2023

References

1. Giustino, F. Electron-phonon interactions from first principles. *Rev. Mod. Phys.* **89**, 015003 (2017).
2. Alexandrov, A. S. & Devreese, J. T. *Advances in Polaron Physics*. Vol. 159 (Springer, 2010).
3. Born, M. & Huang, K. *Dynamical Theory of Crystal Lattices*. (Clarendon Press, 1954).
4. Wright, A. D. et al. Electron–phonon coupling in hybrid lead halide perovskites. *Nat. Commun.* **7**, 11755 (2016).
5. Oberhofer, H., Reuter, K. & Blumberger, J. Charge transport in molecular materials: an assessment of computational methods. *Chem. Rev.* **117**, 10319–10357 (2017).
6. Franchini, C., Reticcioli, M., Setvin, M. & Diebold, U. Polarons in materials. *Nat. Rev. Mater.* **6**, 560–586 (2021).
7. Coropceanu, V. et al. Hole- and electron-vibrational couplings in oligoacene crystals: intramolecular contributions. *Phys. Rev. Lett.* **89**, 275503 (2002).
8. Coropceanu, V. et al. Charge transport in organic semiconductors. *Chem. Rev.* **107**, 926–952 (2007).
9. Sánchez-Carrera, R. S., Paramonov, P., Day, G. M., Coropceanu, V. & Brédas, J.-L. Interaction of charge carriers with lattice vibrations in oligoacene crystals from naphthalene to pentacene. *J. Am. Chem. Soc.* **132**, 14437–14446 (2010).
10. Fratini, S., Ciuchi, S., Mayou, D., De Laissardière, G. T. & Troisi, A. A map of high-mobility molecular semiconductors. *Nat. Mater.* **16**, 998–1002 (2017).
11. Atxabal, A. et al. Tuning the charge flow between Marcus regimes in an organic thin-film device. *Nat. Commun.* **10**, 2089 (2019).
12. Panhans, M. et al. Molecular vibrations reduce the maximum achievable photovoltage in organic solar cells. *Nat. Commun.* **11**, 1488 (2020).
13. Ortmann, F., Bechstedt, F. & Hannewald, K. Theory of charge transport in organic crystals: beyond Holstein's small-polaron model. *Phys. Rev. B* **79**, 235206 (2009).
14. Fratini, S., Mayou, D. & Ciuchi, S. The transient localization scenario for charge transport in crystalline organic materials. *Adv. Funct. Mater.* **26**, 2292–2315 (2016).
15. Nematiaram, T. & Troisi, A. Modeling charge transport in high-mobility molecular semiconductors: Balancing electronic structure and quantum dynamics methods with the help of experiments. *J. Chem. Phys.* **152**, 190902 (2020).
16. Schweicher, G. et al. Molecular semiconductors for logic operations: dead-end or bright future? *Adv. Mater.* **32**, 1905909 (2020).
17. Goodvin, G. L., Mishchenko, A. S. & Berciu, M. Optical conductivity of the Holstein polaron. *Phys. Rev. Lett.* **107**, 76403 (2011).
18. Bonča, J. & Trugman, S. A. Dynamic properties of a polaron coupled to dispersive optical phonons. *Phys. Rev. B* **103**, 54304 (2021).
19. Li, W., Ren, J. & Shuai, Z. A general charge transport picture for organic semiconductors with nonlocal electron-phonon couplings. *Nat. Commun.* **12**, 4260 (2021).
20. De Filippis, G., Cataudella, V., Mishchenko, A. S. & Nagaosa, N. Optical conductivity of polarons: Double phonon cloudconcept verified by diagrammatic Monte Carlo simulations. *Phys. Rev. B* **85**, 94302 (2012).
21. Ishii, H., Honma, K., Kobayashi, N. & Hirose, K. Wave-packet approach to transport properties of carrier coupled with intermolecular and intramolecular vibrations of organic semiconductors. *Phys. Rev. B* **85**, 245206 (2012).
22. Mishchenko, A. S., Nagaosa, N., De Filippis, G., de Candia, A. & Cataudella, V. Mobility of Holstein polaron at finite temperature: an unbiased approach. *Phys. Rev. Lett.* **114**, 146401 (2015).
23. Bonča, J., Trugman, S. A. & Berciu, M. Spectral function of the Holstein polaron at finite temperature. *Phys. Rev. B* **100**, 94307 (2019).
24. Giannini, S. et al. Quantum localization and delocalization of charge carriers in organic semiconducting crystals. *Nat. Commun.* **10**, 3843 (2019).
25. Nematiaram, T., Ciuchi, S., Xie, X., Fratini, S. & Troisi, A. Practical computation of the charge mobility in molecular semiconductors using transient localization theory. *J. Phys. Chem. C* **123**, 6989–6997 (2019).
26. Nematiaram, T., Padula, D., Landi, A. & Troisi, A. On the largest possible mobility of molecular semiconductors and how to achieve it. *Adv. Funct. Mater.* **30**, 2001906 (2020).
27. Fetherolf, J. H., Golež, D. & Berkelbach, T. C. A unification of the holstein polaron and dynamic disorder pictures of charge transport in organic crystals. *Phys. Rev. X* **10**, 21062 (2020).
28. Ciuchi, S., Fratini, S. & Mayou, D. Transient localization in crystalline organic semiconductors. *Phys. Rev. B* **83**, 81202 (2011).
29. Holstein, T. Studies of polaron motion, part I. *Ann. Phys.* **8**, 325 (1959).
30. Tozer, O. R. & Barford, W. Localization of large polarons in the disordered Holstein model. *Phys. Rev. B - Condens. Matter Mater. Phys.* **89**, 155434 (2014).
31. Holstein, T. Studies of polaron motion: part II. The "small" polaron. *Ann. Phys.* **8**, 343–389 (1959).
32. Jortner, J. Temperature dependent activation energy for electron transfer between biological molecules. *J. Chem. Phys.* **64**, 4860–4867 (1976).
33. Silbey, R. & Munn, R. W. General theory of electronic transport in molecular crystals. I. Local linear electron-phonon coupling. *J. Chem. Phys.* **72**, 2763–2773 (1980).
34. Munn, R. W. & Silbey, R. Theory of electronic transport in molecular crystals. II. Zeroth order states incorporating nonlocal linear electron-phonon coupling. *J. Chem. Phys.* **83**, 1843–1853 (1985).
35. Marcus, R. A. Electron transfer reactions in chemistry. Theory and experiment. *Rev. Mod. Phys.* **65**, 599–610 (1993).
36. Hannewald, K. et al. Theory of polaron bandwidth narrowing in organic molecular crystals. *Phys. Rev. B* **69**, 075211 (2004).
37. Lu, T. & Dunlap, D. H. Band narrowing in semiclassical nonadiabatic electron transfer. *Phys. Rev. B - Condens. Matter Mater. Phys.* **67**, 012301 (2003).
38. Giannini, S. & Blumberger, J. Charge transport in organic semiconductors: the perspective from nonadiabatic molecular dynamics. *Acc. Chem. Res.* **55**, 819–830 (2022).
39. Hutsch, S., Panhans, M. & Ortmann, F. Time-consistent hopping transport with vibration-mode-resolved electron-phonon couplings. *Phys. Rev. B* **104**, 54306 (2021).
40. Hutsch, S., Panhans, M. & Ortmann, F. Charge carrier mobilities of organic semiconductors: ab initio simulations with mode-specific treatment of molecular vibrations. *npj Comput. Mater.* **8**, 228 (2022).
41. Leggett, A. J. et al. Dynamics of the dissipative two-state system. *Rev. Mod. Phys.* **59**, 1–85 (1987).
42. Kenkre, V. M. & Knox, R. S. Theory of fast and slow excitation transfer rates. *Phys. Rev. Lett.* **33**, 803–806 (1974).
43. Kenkre, V. M., Kühne, R. & Reineker, P. Connection of the velocity autocorrelation function to the mean-square-displacement and to the memory function of generalized master equations. *Z. Phys. B Condens. Matter* **41**, 177–180 (1981).
44. Fan, Z. et al. Linear scaling quantum transport methodologies. *Phys. Rep.* **903**, 1–69 (2021).
45. Kubo, R. Statistical-mechanical theory of irreversible processes. I. *J. Phys. Soc. Jpn.* **12**, 570–586 (1957).
46. Panhans, M. & Ortmann, F. Efficient time-domain approach for linear response functions. *Phys. Rev. Lett.* **127**, 16601 (2021).

47. Weiße, A., Wellein, G., Alvermann, A. & Fehske, H. The kernel polynomial method. *Rev. Mod. Phys.* **78**, 275–306 (2006).
48. Iadonisi, G., Ranninger, J. & De Filippis, G. *Polarons in Bulk Materials and Systems with Reduced Dimensionality*. Vol. 161 (IOS Press, 2006).
49. Bäuml, B., Wellein, G. & Fehske, H. Optical absorption and single-particle excitations in the two-dimensional Holstein t-J model. *Phys. Rev. B* **58**, 3663–3676 (1998).
50. Fehske, H., Loos, J. & Wellein, G. Lattice polaron formation: effects of nonscreened electron-phonon interaction. *Phys. Rev. B* **61**, 8016–8025 (2000).
51. Vandewal, K. et al. Absorption tails of donor:C_{60} blends provide insight into thermally activated charge-transfer processes and polaron relaxation. *J. Am. Chem. Soc.* **139**, 1699–1704 (2017).
52. Ruggiero, M. T., Zeitler, J. A. & Erba, A. Intermolecular anharmonicity in molecular crystals: interplay between experimental low-frequency dynamics and quantum quasi-harmonic simulations of solid purine. *Chem. Commun.* **53**, 3781–3784 (2017).
53. Asher, M. et al. Anharmonic lattice vibrations in small-molecule organic semiconductors. *Adv. Mater.* **32**, 1908028 (2020).
54. Yaffe, O. et al. Local polar fluctuations in lead halide perovskite crystals. *Phys. Rev. Lett.* **118**, 136001 (2017).
55. Mayers, M. Z., Tan, L. Z., Egger, D. A., Rappe, A. M. & Reichman, D. R. How lattice and charge fluctuations control carrier dynamics in halide perovskites. *Nano Lett.* **18**, 8041–8046 (2018).
56. Brown, D. W., Romero, A. H. & Lindenberg, K. Franck-condon factors as spectral probes of polaron structure. *J. Phys. Chem. A* **103**, 10417–10425 (1999).
57. Cheng, Y. C. & Silbey, R. J. A unified theory for charge-carrier transport in organic crystals. *J. Chem. Phys.* **128**, 114713 (2008).
58. Mahan, G. D. *Many-Particle Physics*, *Third Edition*. (Plenum, 2000).
59. Bursill, R. J., McKenzie, R. H. & Hamer, C. J. Phase diagram of the one-dimensional Holstein model of spinless fermions. *Phys. Rev. Lett.* **80**, 5607–5610 (1998).
60. Capone, M. & Ciuchi, S. Polaron crossover and bipolaronic metal-insulator transition in the half-filled Holstein model. *Phys. Rev. Lett.* **91**, 186405 (2003).
61. Sykora, S., Hübsch, A., Becker, K. W., Wellein, G. & Fehske, H. Single-particle excitations and phonon softening in the one-dimensional spinless Holstein model. *Phys. Rev. B* **71**, 45112 (2005).
62. Marini, G. & Calandra, M. Lattice dynamics of photoexcited insulators from constrained density-functional perturbation theory. *Phys. Rev. B* **104**, 144103 (2021).
63. Berlin, Y. A., Burin, A. L., Siebbeles, L. D. A. & Ratner, M. A. Conformationally gated rate processes in biological macromolecules. *J. Phys. Chem. A* **105**, 5666–5678 (2001).
64. Yang, H., Gajdos, F. & Blumberger, J. Intermolecular charge transfer parameters, electron-phonon couplings, and the validity of polaron hopping models in organic semiconducting crystals: rubrene, pentacene, and C60. *J. Phys. Chem. C* **121**, 7689–7696 (2017).
65. Newton, M. D. & Sutin, N. Electron transfer reactions in condensed phases. *Annu. Rev. Phys. Chem.* **35**, 437–480 (1984).

Acknowledgements

We would like to thank the Deutsche Forschungsgemeinschaft for financial support [CRC1415, projects No. OR 349/11 and No. OR 349/3 and the Cluster of Excellence e-conversion (Grant no. EXC2089)]. Grants for computer time from the Zentrum für Informationsdienste und Hochleistungsrechnen of TU Dresden and the Leibniz Supercomputing Centre in Garching are gratefully acknowledged.

Author contributions

M.P. has performed the theoretical calculations. M.P., S.H., and F.O. have developed the theoretical model. M.P. and F.O. have written the paper. F.O. has supervised the study.

Funding

Open Access funding enabled and organized by Projekt DEAL.

Competing interests

The authors declare no competing interests.

Additional information

Supplementary information The online version contains supplementary material available at https://doi.org/10.1038/s42005-023-01241-w.

Correspondence and requests for materials should be addressed to Frank Ortmann.

Peer review information *Communications Physics* thanks the anonymous reviewers for their contribution to the peer review of this work.

Reprints and permission information is available at http://www.nature.com/reprints

Publisher's note Springer Nature remains neutral with regard to jurisdictional claims in published maps and institutional affiliations.